Biophysical Journal, Volume *120*

Supplemental information

Stochastic reaction-diffusion modeling of calcium dynamics in 3D dendritic spines of Purkinje cells

Victor Nicolai Friedhoff, Gabriela Antunes, Martin Falcke, and Fabio M. Simões de Souza

Manuscript submitted to **Biophysical***Journal*
Article

Supporting Material to Stochastic reaction-diffusion modeling of calcium dynamics in 3D-dendritic spines of Purkinje Cells

Victor Nicolai Friedhoff[1,2], Gabriela Antunes[3], Martin Falcke[1,2], and Fabio M. Simões de Souza[3,a]

[1]Mathematical Cell Physiology, Max Delbrück Center for Molecular Medicine, Berlin, Germany
[2]Department of Physics, Humboldt University, Berlin, Germany
[3]Center for Mathematics, Computation, and Cognition, Federal University of ABC, São Bernardo do Campo, SP, Brasil
[a]Correspondence: fabio.souza@ufabc.edu.br

1 SUPPORTING MATERIAL

1.1 Simulation methods

We constructed the three-dimensional geometry of a dendritic spine in Blender, a free open-source software used to create three-dimensional geometries (1). We then used CellBlender to incorporate the dendrite's geometry with the biophysical model and MCell 3.4 (2–4) to run stochastic simulations. MCell is a stochastic single particle simulator of reaction-diffusion systems in three dimensions. All particles are tracked over variable time steps and diffuse by a discrete random walk through a predefined volume using ray-tracing techniques. The length of each spatial step during the random walk is determined by the diffusion constant of the particle species and the current time step. Particles can be set to diffuse on predefined surfaces or in volumes. Reactions of particle species can be specified by first- and second-order reaction kinetics, resp. Ray-marching is used to propagate rays after collisions and Monte Carlo probabilities are used to decide about triggering reactions. When two particles are close enough, MCell determines the reaction probabilities in dependence on the specific reaction rates, a set of predefined random numbers ('seeds'), and time step which then leads to stochastic reaction events.

The positions of all particles, including IP_3R, SERCA, and leak channel molecules on the ER membrane and PMCA, NCX, and leak channel molecules on the spine membrane depend on the used seed, i.e. are randomly chosen individually for each simulation run.

In parallel, we modeled the system's Ca^{2+} response in terms of coupled ordinary differential equations (ODEs) describing average particle concentrations using Copasi (5). While MCell offers a biophysically realistic approach to a biological problem, accounting for low particle concentrations, inherent stochasticity and complex three-dimensional geometries (6), Copasi describes the kinetic reactions in a well-mixed volume efficiently, without the influence of diffusion or complex geometry. In this way, the dynamics of the model can be tested in a computationally fast environment before going into more expensive reaction-diffusion simulations in complex geometries. Copasi was for instance used to approximately find concentrations of each species at equilibrium, i.e. the initial state. An overview over different deterministic and stochastic simulation tools used in computation biology can be found in (7).

We chose one spatial compartment with the same volume as in MCell with $V_{compartment} = 0.512\ \mu m^3$ in Copasi to have an agreeing notion of concentrations and particle numbers, but did not account for any kind of complex geometry. Dynamics were modeled in terms of spatially homogeneous deterministic concentrations of particle species, described by a set of coupled ODEs in contrast to stochastic interactions of single particles diffusing in a complex volume in MCell.

1.2 IP_3R Receptor models

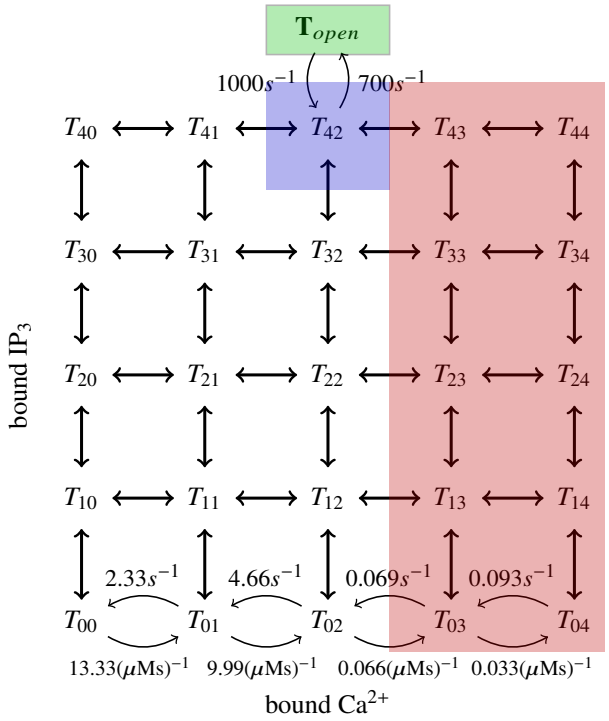

Figure S1: Extended visualisation of Moraru's IP_3R model.

(left) Subsection of Moraru's IP_3R model with example rates shown for binding and unbinding of Ca^{2+} and transition in to and from open state T_{open}. When four IP_3 and two Ca^{2+} (activating) are bound, T_{42} (blue), there is a probability to go into the open state T_{open} (green), whence additional Ca^{2+} will be released. Further Ca^{2+} binding of the IP_3R will lower the probability of opening, effectively promoting the ten states T_{x3} and T_{x4} to inhibitory Ca^{2+} states (red), $x \in [0, 4]$.

(right) Table of parameters used for Moraru's IP_3R model. The reaction rates of binding Ca^{2+} or IP_3 are proportional to the available binding sites, while dissociation rates are proportional to the number of bound Ca^{2+} or IP_3. We get e.g. $T_{4x} \rightarrow T_{3x} + IP_3$ with $k = 4 \cdot k_{IP3\text{-}Off} = 4 \cdot 25s^{-1} = 100s^{-1}$ because there are 4 independently bound IP_3 that can trigger the decay into state T_{3x}. Additionally, we set the Ca^{2+} binding and dissociation rates of the inhibitory states to be slower than into or from the activating states, expressed by the scaling ratio r_s. We get e.g. $T_{x2} + Ca^{2+} \rightarrow T_{x3}$ with $k = 2 \cdot r_s \cdot k_{CaOn} = 2 \cdot 0.01 \cdot 3.3\ (\mu Ms)^{-1} = 0.066\ (\mu Ms)^{-1}$.

Moraru's IP_3R model

reactions		on rate	off rate
	excitatory		
$T_{x0} + Ca^{2+}$	$\leftrightarrow T_{x1}$	13.33 $(\mu M\ s)^{-1}$	2.33 s^{-1}
$T_{x1} + Ca^{2+}$	$\leftrightarrow T_{x2}$	9.99 $(\mu M\ s)^{-1}$	4.66 s^{-1}
	inhibitory	(here r_s=0.01)	
$T_{x2} + Ca^{2+}$	$\leftrightarrow T_{x3}$	0.066 $(\mu M\ s)^{-1}$	0.069 s^{-1}
$T_{x3} + Ca^{2+}$	$\leftrightarrow T_{x4}$	0.033 $(\mu M\ s)^{-1}$	0.093 s^{-1}
	IP_3		
$T_{0x} + IP_3$	$\leftrightarrow T_{1x}$	333.33 $(\mu M\ s)^{-1}$	25 s^{-1}
$T_{1x} + IP_3$	$\leftrightarrow T_{2x}$	249.99 $(\mu M\ s)^{-1}$	50 s^{-1}
$T_{2x} + IP_3$	$\leftrightarrow T_{3x}$	166.66 $(\mu M\ s)^{-1}$	75 s^{-1}
$T_{3x} + IP_3$	$\leftrightarrow T_{4x}$	83.33 $(\mu M\ s)^{-1}$	100 s^{-1}
	opening		
T_{42}	$\leftrightarrow T_{open}$	700 s^{-1}	1000 s^{-1}
T_{open}	$\rightarrow Ca^{2+}$ release	10000 s^{-1}	

Table S1: Table with parameter values used for Moraru's IP_3R model (8).

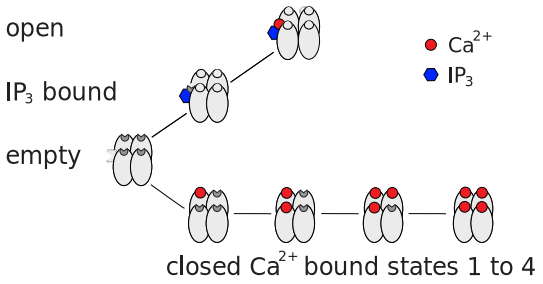

Figure S2: Extended visualisation of Doi's IP_3R model

Doi's IP_3R model

reactions		on rate	off rate
$IP3R_o$	$\rightarrow Ca^{2+}$ release	5400 s^{-1}	
$IP3R_i + Ca^{2+}$	$\leftrightarrow IP3R_o$	8000 $(\mu M\ s)^{-1}$	2000 s^{-1}
$IP3R + IP_3$	$\leftrightarrow IP3R_i$	1000 $(\mu M\ s)^{-1}$	25800 s^{-1}
$IP3R + Ca^{2+}$	$\leftrightarrow IP3R_{c1}$	8.88 $(\mu M\ s)^{-1}$	5 s^{-1}
$IP3R_{c1} + Ca^{2+}$	$\leftrightarrow IP3R_{c2}$	19.98 $(\mu M\ s)^{-1}$	10 s^{-1}
$IP3R_{c2} + Ca^{2+}$	$\leftrightarrow IP3R_{c3}$	39.96 $(\mu M\ s)^{-1}$	15 s^{-1}
$IP3R_{c3} + Ca^{2+}$	$\leftrightarrow IP3R_{c4}$	59.94 $(\mu M\ s)^{-1}$	20 s^{-1}

Table S2: Reaction rates used for Doi's IP_3R model (9).

(left) IP_3R model from Doi et al. (9). The IP_3Racts as an coincidence detector and only opens if IP_3 attaches before Calcium does. Otherwise it acts as an buffer and goes into the closed states. **(right)** Reaction rates used for Doi's IP_3R model.

1.3 Reaction rates

1.3.1 Buffer rates

Buffer reactions		on rate	off rate	source
Ca^{2+} + Pv	↔ CaPv	107 (μM s)$^{-1}$	0.95 s^{-1}	(10)
Pv	↔ PvMg	472 s^{-1}	25.0 s^{-1}	
Ca^{2+} + Cb	↔ CbCa1	43.5 (μM s)$^{-1}$	35.8 s^{-1}	(11)
CbCa1 + Ca^{2+}	↔ CbCa2	5.5 (μM s)$^{-1}$	2.60 s^{-1}	
Ca^{2+} + CaM	↔ CaM1000	750 (μM s)$^{-1}$	50000 s^{-1}	(12)
Ca^{2+} + CaM	↔ CaM0100	750 (μM s)$^{-1}$	50000 s^{-1}	
Ca^{2+} + CaM	↔ CaM0010	800 (μM s)$^{-1}$	20000 s^{-1}	
Ca^{2+} + CaM	↔ CaM0001	204.6 (μM s)$^{-1}$	5115 s^{-1}	
CaM1000 + Ca^{2+}	↔ CaM1100	750 (μM s)$^{-1}$	625 s^{-1}	
CaM0100 + Ca^{2+}	↔ CaM1100	750 (μM s)$^{-1}$	625 s^{-1}	
CaM0010 + Ca^{2+}	↔ CaM0011	204.6 (μM s)$^{-1}$	25.575 s^{-1}	
CaM0001 + Ca^{2+}	↔ CaM0011	800 (μM s)$^{-1}$	100 s^{-1}	
CaM1000 + Ca^{2+}	↔ CaM1010	800 (μM s)$^{-1}$	20000 s^{-1}	
CaM1000 + Ca^{2+}	↔ CaM1001	204.6 (μM s)$^{-1}$	5115 s^{-1}	
CaM0100 + Ca^{2+}	↔ CaM0110	800 (μM s)$^{-1}$	20000 s^{-1}	
CaM0100 + Ca^{2+}	↔ CaM0101	204.6 (μM s)$^{-1}$	5115 s^{-1}	
CaM0010 + Ca^{2+}	↔ CaM1010	750 (μM s)$^{-1}$	50000 s^{-1}	
CaM0010 + Ca^{2+}	↔ CaM0110	750 (μM s)$^{-1}$	50000 s^{-1}	
CaM0001 + Ca^{2+}	↔ CaM1001	750 (μM s)$^{-1}$	50000 s^{-1}	
CaM0001 + Ca^{2+}	↔ CaM0101	750 (μM s)$^{-1}$	50000 s^{-1}	
CaM1100 + Ca^{2+}	↔ CaM1110	800 (μM s)$^{-1}$	20000 s^{-1}	
CaM1100 + Ca^{2+}	↔ CaM1101	204.6 (μM s)$^{-1}$	5115 s^{-1}	
CaM0011 + Ca^{2+}	↔ CaM1011	750 (μM s)$^{-1}$	50000 s^{-1}	
CaM0011 + Ca^{2+}	↔ CaM0111	750 (μM s)$^{-1}$	50000 s^{-1}	
CaM1010 + Ca^{2+}	↔ CaM1110	750 (μM s)$^{-1}$	625 s^{-1}	
CaM0110 + Ca^{2+}	↔ CaM1110	750 (μM s)$^{-1}$	625 s^{-1}	
CaM1001 + Ca^{2+}	↔ CaM1101	750 (μM s)$^{-1}$	625 s^{-1}	
CaM0101 + Ca^{2+}	↔ CaM1101	750 (μM s)$^{-1}$	625 s^{-1}	
CaM1010 + Ca^{2+}	↔ CaM1011	204.6 (μM s)$^{-1}$	25.575 s^{-1}	
CaM0110 + Ca^{2+}	↔ CaM0111	204.6 (μM s)$^{-1}$	25.575 s^{-1}	
CaM1001 + Ca^{2+}	↔ CaM1011	800 (μM s)$^{-1}$	100 s^{-1}	
CaM0101 + Ca^{2+}	↔ CaM0111	800 (μM s)$^{-1}$	100 s^{-1}	
CaM1110 + Ca^{2+}	↔ CaM1111	204.6 (μM s)$^{-1}$	25.575 s^{-1}	
CaM1101 + Ca^{2+}	↔ CaM1111	800 (μM s)$^{-1}$	100 s^{-1}	
CaM1011 + Ca^{2+}	↔ CaM1111	750 (μM s)$^{-1}$	625 s^{-1}	
CaM0111 + Ca^{2+}	↔ CaM1111	750 (μM s)$^{-1}$	625 s^{-1}	

Table S3: Rates used for buffer reactions. Rates of Fluo-5F were chosen according to their K_d and concentrations (13).

1.3.2 Ca^{2+} transporter and IP_3 reaction rates

Reaction		on rate	off rate	source
PMCA + Ca^{2+}	$\leftrightarrow$ PMCA1	2500 $(\mu M\ s)^{-1}$	2000 s^{-1}	(12, 14)
PMCA1	$\rightarrow$ PMCA	125 s^{-1}		(12)
SERCA + Ca^{2+}	$\leftrightarrow$ SERCA1	17147 $(\mu M\ s)^{-1}$	8426.3 s^{-1}	(12, 15)
SERCA1 + Ca^{2+}	$\leftrightarrow$ SERCA2	17147 $(\mu M\ s)^{-1}$	8426.3 s^{-1}	(12, 15)
SERCA2	$\rightarrow$ SERCA	250 s^{-1}		(16)
NCX + Ca^{2+}	$\leftrightarrow$ NCX1	800 $(\mu M\ s)^{-1}$	100 s^{-1}	(12)
NCX1	$\rightarrow$ NCX	2300 s^{-1}		(12)
Leak ER	Ca^{2+} release	26 s^{-1}		us
Leak Den	Ca^{2+} release	26 s^{-1}		us
$IP3_{caged}$	$\rightarrow$ IP3	7 s^{-1}		us
IP3	$\rightarrow$ NULL	15 s^{-1}		us

Table S4: Reaction rates for Ca^{2+} transporters and leaks, as well as rates for decay of caged IP_3 to IP_3 and degradation of IP_3.

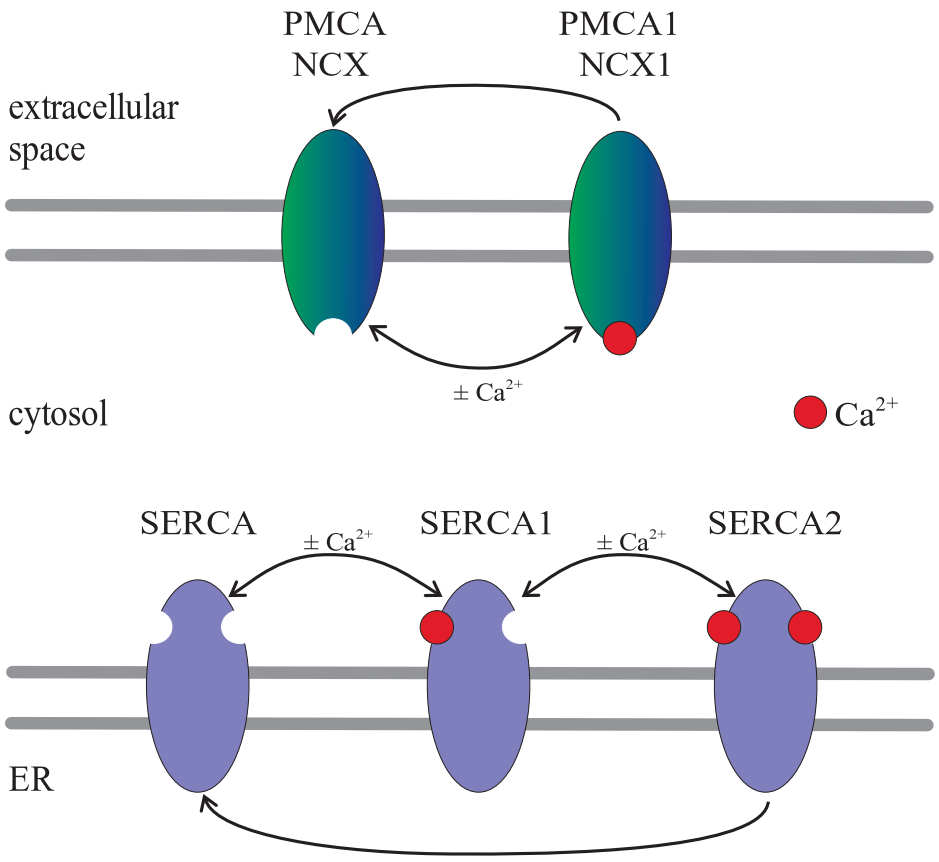

Figure S3: Graphical representation of SERCA, PMCA and NCX models used. Double-headed arrows indicate binding and unbinding of Ca^{2+}, while one-headed arrows indicate decay (removal of Ca^{2+}).

1.4 Geometry

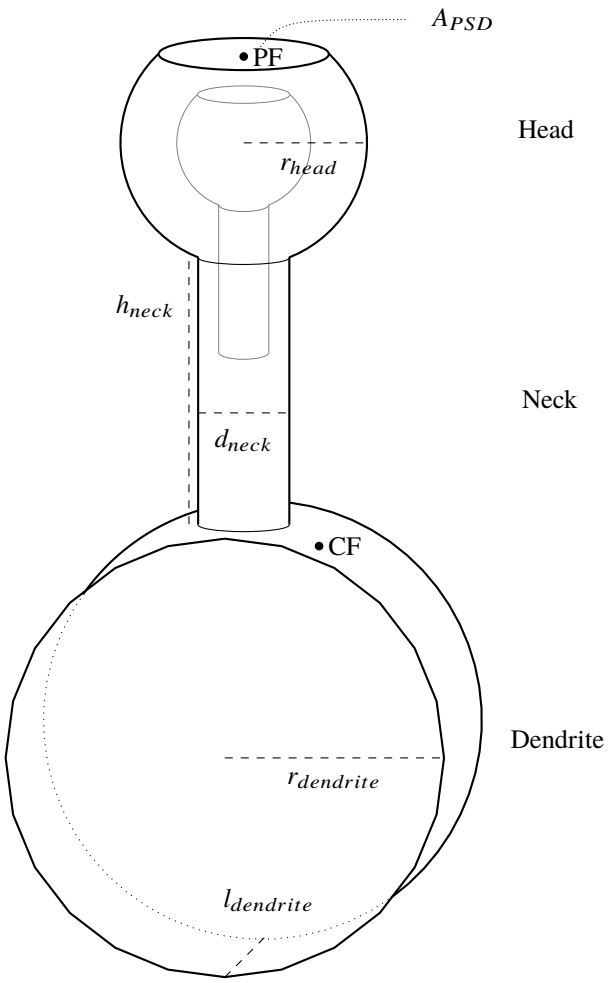

Spatial parameters

Segment		Volume in μm^3
Spine head	V_{head}	0.100
Spine neck	V_{neck}	0.021
Dendrite	$V_{dendrite}$	0.391
Total volume	V	0.512
ER head	$V_{ER,head}$	0.017
ER neck	$V_{ER,neck}$	0.003
ER volume	V_{ER}	0.020
Segment		Area in μm^2
PSD	A_{PSD}	0.152
ER surface	A_{ER}	0.445
Segment		Length in μm
PSD Radius	r_{PSD}	0.22
Spine head radius	r_{head}	0.30
Spine neck diameter	d_{neck}	0.20
Spine neck height	h_{neck}	0.58 to 0.60
ER head radius	$r_{ER,head}$	0.163
ER neck height	$r_{ER,neck}$	0.33
Dendrite radius	$r_{dendrite}$	0.50
Dendrite length	$l_{dendrite}$	0.50

Figure S4: Spatial parameters of geometry based on measurements from (17), created in Blender (1).

For the calculation of particle concentrations in the spine head we used the volume of the cytosolic part of the spine head, $V_{head,\,cytosol} \approx 0.082 \mu m^3$, therefore 50 particles $\approx 1\ \mu$M.

During Ca^{2+} transients, the spine head traps Ca^{2+} and thereby acts as a sink. While the concentration in the spine head is approximately constant, it decreases linearly along the length of the neck down the z-axis, until it is constant again in the dendrite element. An example of this is shown in Movie S5, where the geometry was cut into 200 slices along the z-axis and Ca^{2+} in these slices was plotted against the z-axis in the geometry.

1.5 Particle concentrations and diffusion coefficients

Molecule	concentration	# of molecules	source	diffusion coefficient	source
Calcium (Ca^{2+})	50nM	15	(18, 19)	223 $\mu m^2 s^{-1}$	(11, 20)
Inositol trisphosphate (IP_3)				10 $\mu m^2 s^{-1}$	(21)
caged IP_3		1400		280 $\mu m^2 s^{-1}$	us
Parvalbumin (PV)	40μM	11845	(19)	43 $\mu m^2 s^{-1}$	(11)
Calbindin (Cb)	40μM	11845	(19)	28 $\mu m^2 s^{-1}$	(11)
Calmodulin (CaM)	19μM	5625	(16, 22)	25 $\mu m^2 s^{-1}$ empty, 2.5 $\mu m^2 s^{-1}$ Ca^{2+} bound	
Magnesium (Mg^{2+})	590μM		(11)		
IP_3R Doi's model		60	estimated, (23)		
IP_3R Moraru's model		52, 54, 56	estimated, (23)		
SERCA		68	(16)		
PMCA		13	(16)		
NCX		5	(16)		
Dendrite Leak		10			
ER Leak		10			

Table S5: Total and basal concentrations, particle numbers, and diffusion coefficients of particle species. Mg^{2+} and Fluo-5F were not modeled explicitly, but only as part of pseudo first-order reactions. Ca^{2+} transporters were set to be unmovable. Caged IP_3 was confined to a small box volume in the PSD, only free IP_3 was allowed to leave that box.

Subspecies concentrations for the basal state s.t. $[Ca^{2+}_{free}] \approx 50$nM in equilibrium as determined in Copasi are

Species	Total #	Substates	#
Free Ca^{2+}	15		
PV	11845	PV	464
		PVCa	2619
		PVMg	8760
Cb	11845	Cb	11112
		CbCa1	677
		CbCa2	71
CaM	5625	CaM	5592
		CaM0001	11
		CaM0010	11
		CaM0100	4
		CaM1000	3
		CaM0011	4
SERCA	68	SERCA	61
		SERCA1	6
		SERCA2	1
PMCA	13	PMCA	12
		PMCA1	1
NCX	5	NCX	5

Table S6: Particle numbers of subspecies at steady state.

All other substates did not occur in the basal state.

1.6 Results - Doi's IP_3R model

1.6.1 MCell

See results section 3.1 on Doi's model and Fig. S5.

1.6.2 Copasi

We included Doi's IP_3R model (9), buffers and Ca^{2+} transporters into one compartment in Copasi and studied the Ca^{2+} transients in response to different Ca^{2+} amplitudes of the PF and CF stimuli for the cases of PF burst and PF burst + CF. We used up-to-date parameter values that differ from Doi et al. to agree with current literature and to be able to create Ca^{2+} transients of similar properties.

The peak of the Ca^{2+} transient weakly depends on the Ca^{2+} amplitude of the PF burst stimulus, Fig. S6, when no CF stimulus is present. Without changing $[IP_3](t)$ the peak value of the transient increases from about $p(PF = 0\mu M) = 1.6\mu M$ to saturating at $p(PF > 0.4\mu M) = 1.8\mu M$, an increase of about 12.5%.

When we choose one PF Ca^{2+} amplitude per spike of the PF burst, e.g. $PF = 0.25\mu M$, and add a CF stimulus, we can scale the peak of the resulting Ca^{2+} transient by changing the Ca^{2+} amplitude of the CF stimulus, Fig. S7. The transient shows no peak saturation for low to medium CF Ca^{2+} amplitudes. We can scale the peak from $p(CF = 0) = 1.8\mu M$ to e.g. $p(CF = 6\mu M) = 9\mu M$, Fig. S7, an increase of about 500%, way beyond the 150% required as estimated from experimental data (13).

1.7 Results - Moraru's IP_3R model

1.7.1 Copasi

We replaced Doi's IP_3R model by Moraru's IP_3R model, computed a new steady state, and subjected the system to the same PF and CF stimuli. We find that the system reacts much more sensitively to Ca^{2+} input coming from either PF or CF stimuli. For PF stimuli, there is no convergence of transients for low to intermediate PF Ca^{2+} amplitudes compared to Doi, Fig. S6. The maximal scaling also increases by about a factor of 5 for the stimuli chosen in Fig. S8, with the peak around $p(PF = 0) = 0.3\mu M$ to $p(PF = 0.3\mu M) = 1.6\mu M$. When adding a CF stimulus to the PF burst we can influence the resulting Ca^{2+} transient easily. Even for small values of CF Ca^{2+} amplitude (compared to the results with Doi's model, Fig. S7), we can increase the Ca^{2+} response massively from about 1.5 μM without CF stimulus to 9 μM with CF = 0.8 μM, Fig. S9.

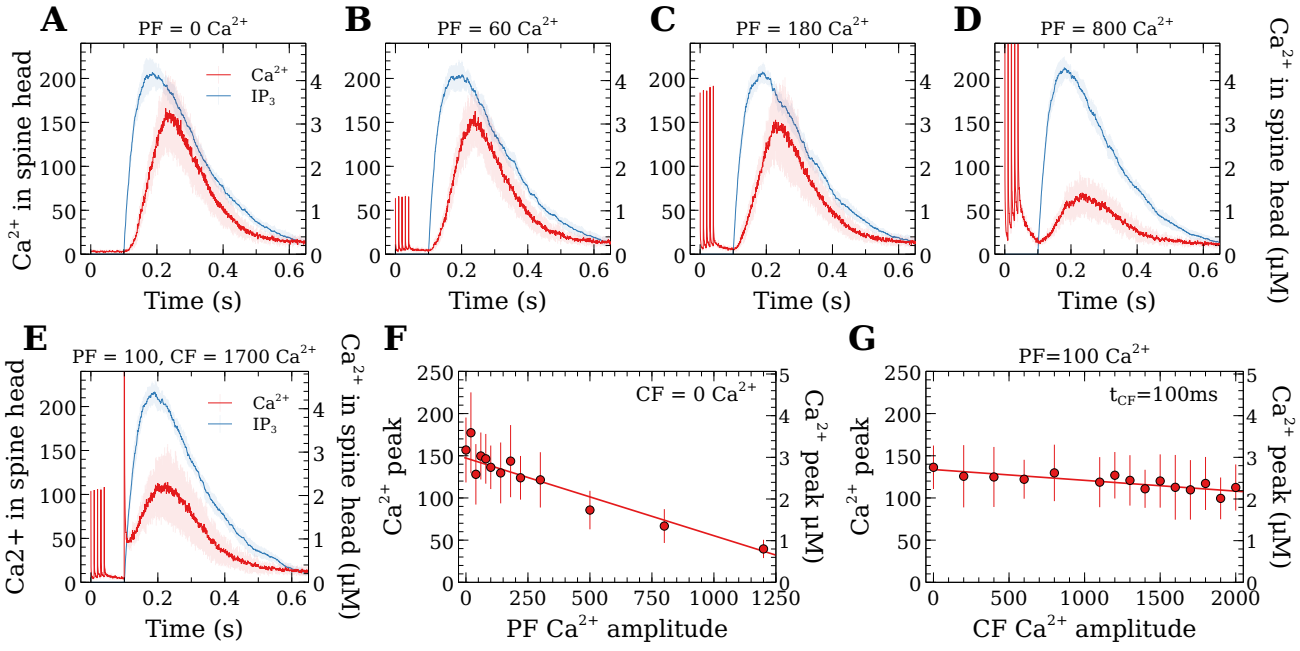

Figure S5: **(A-D)** IP_3R induced Ca^{2+} transients using Doi's IP_3R model in MCell in response to PF burst stimulus of variable Ca^{2+} amplitude a) PF=0 Ca^{2+}, b) PF=60 Ca^{2+}, c) PF=180 Ca^{2+}, d) PF=800 Ca^{2+}. Plots are averages (red Ca^{2+}, blue IP_3) and standard deviations (opaque areas) of 12 stochastic simulations. **(E)** Example IP_3R induced Ca^{2+} transient (red) from PF burst stimulus with CF coactivation at $t_{CF} = 100\ ms$ with PF=100 Ca^{2+} and CF=1700 Ca^{2+}, and IP_3 (blue). **(F)** Ca^{2+} transient peak values for a large range of PF Ca^{2+} amplitudes without CF coactivation. **(G)** Ca^{2+} transient peak values for a large range of CF Ca^{2+} amplitudes with $t_{CF} = 100\ ms$ for PF burst + CF stimulation. Parameters not explicitly mentioned are given in Table S2. Data points in (F) and (G) are averages of 12 simulations each, error bars indicate standard deviations.

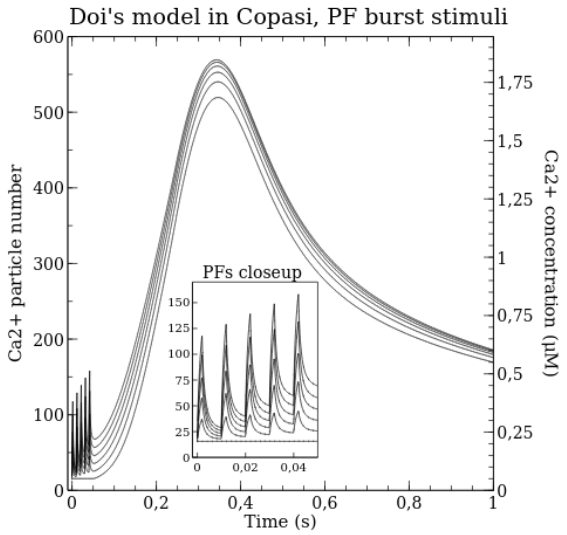

Figure S6: Doi's model, Ca^{2+} transients with different Ca^{2+} per PF spike, 0 (yielding the smallest Ca^{2+} transient) to approximately 0.4μM (yielding the largest Ca^{2+} transient). Increasing Ca^{2+} from PF spikes does increase the peak of the Ca^{2+} transient, but saturates at about 1.8μM. Closeup of PF spikes is visible in the smaller plot.

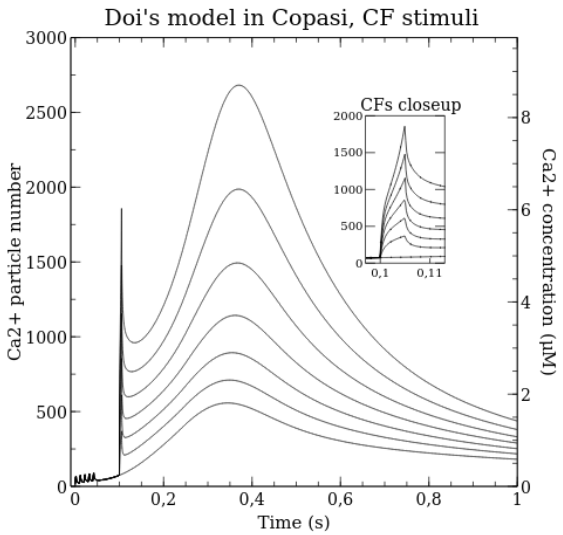

Figure S7: Doi's model, Ca^{2+} transient with different Ca^{2+} per CF stimulus and closeup of CF Ca^{2+} spikes. The peak of the Ca^{2+} transient depends strongly on the Ca^{2+} amplitude of the CF stimulus. We can scale the peak from $p(CF = 0) = 1.8\mu$M to e.g. $p(CF = 6\mu\text{M}) = 9\mu$M, an increase of about 500%.

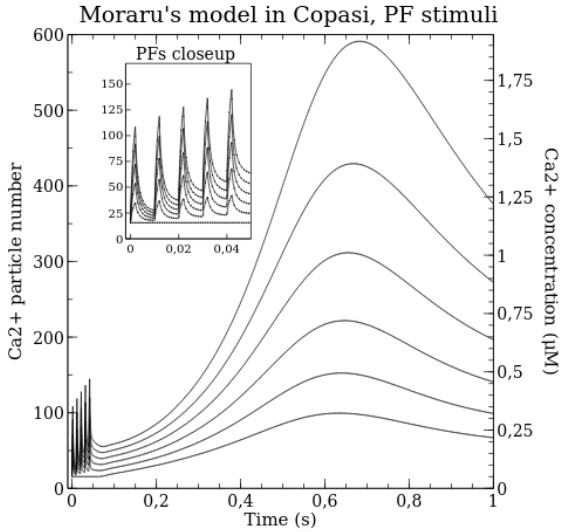

Figure S8: Moraru's model, Ca^{2+} transient with different Ca^{2+} per one PF stimulus, 0 to 0.4uM. Increasing PF Ca^{2+} amplitude clearly increases the peak of the Ca^{2+} transient. There is no saturation at low to intermediate PF Ca^{2+} amplitudes and the transient reacts more sensitively to PF stimuli, showing an peak increase of about 500% from no PF stimulus to an PF Ca^{2+} amplitude of about 0.4μM.

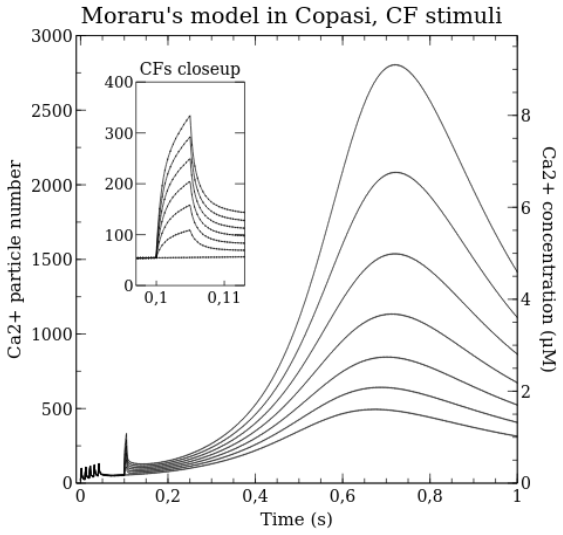

Figure S9: Moraru's model, Ca^{2+} transient for a chosen constant PF Ca^{2+} amplitude of PF=0.25 μM and variable CF Ca^{2+} amplitudes. In comparison to Doi's model, Moraru's model requires much smaller CF Ca^{2+} amplitudes to reach higher peak values of the resulting Ca^{2+} transient. An increase of the Ca^{2+} transient's peak value of 150% with CF coactivation following experimental data from Piochon et al (13) is easily archived.

1.7.2 Comparison to optimal time window data by Wang et al.

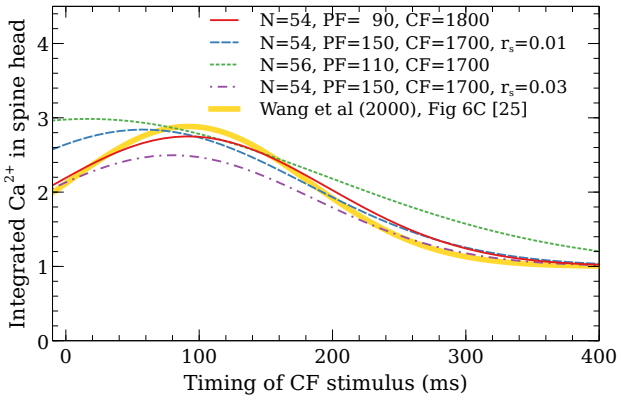

Figure S10: Integral from 0.1s to 0.8s of Ca^{2+} transients against timing of CF stimulus for the same data as in Fig. 8. We plot the Gaussian fits to the data points only. We compare them with the Gaussian which was fit to the experimental data by Wang et al. in (24). The blue (green) set is set B (C) in Fig. 6. A rather small change of parameter values (red) leads to good agreement with the experimental results from Wang et al. (24).

1.7.3 Buffers

Buffers modulate the amplitude of the free Ca^{2+} transient. We studied the Ca^{2+} peak amplitude modulation of the buffer species Pv, CaM, and Cb by removing them individually and ran simulations with a PF burst and a PF burst + CF stimulus.

Removing any buffer species led to an increase of the Ca^{2+} transient peak value with Pv having the weakest effect for both cases with and without CF coactivation. Its Ca^{2+} binding site (K_d = 8.8 nM) is occupied mainly by Mg^{2+} at the resting Ca^{2+} concentration of 50 nM. Ca^{2+} replaces Mg^{2+} (see Fig. S11A) with increasing concentration and is buffered that way by Pv. Therefore Pv becomes more relevant for higher [Ca^{2+}] only.

We find that Cb has the strongest effect on peak values, followed by CaM and then Pv, Fig. S11A. This is in agreement with buffer concentrations ([Cb]=40 μM, [CaM]=19 μM) and the dissociation constants K_d for the different Ca^{2+} binding sites of CaM (K_d = 0.125 μM to 66.6 μM) and Cb (K_d = 0.473 μM to 0.823 μM).

Additionally, our results show that buffers do not only influence Ca^{2+} transient peak values, but also positive and negative feedback of Ca^{2+} on IP_3Rs. Fig. S11B shows the average of the total number of released Ca^{2+}. Removing Cb has the strongest influence for a PF burst again and yields a very strong increase in IP_3R Ca^{2+} release. It almost reaches the release of the PF burst + CF coactivation scenario with all buffer species present. Once the CF stimulus has happened, the differences between the four scenarios is less prominent, but removing Cb still increases IP_3R activity the most.

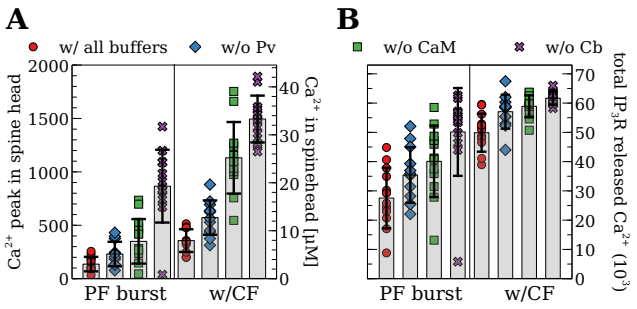

Figure S11: **(A)** Peaks of Ca^{2+} transients from simulations with different buffer contents. Full circles (red) are peak values of Ca^{2+} transients with all three buffer species included, while the rest show peak values for cases with either Pv, CaM, or Cb removed. **(B)** Total number of Ca^{2+} released from IP_3Rs with either all buffers included or one buffer species removed, same color and symbol scheme as in A. Individual symbols show the 12 simulations which were used to calculate averages and standard deviations, shown as bars.

1.7.4 Single PF stimulus with CF coactivation

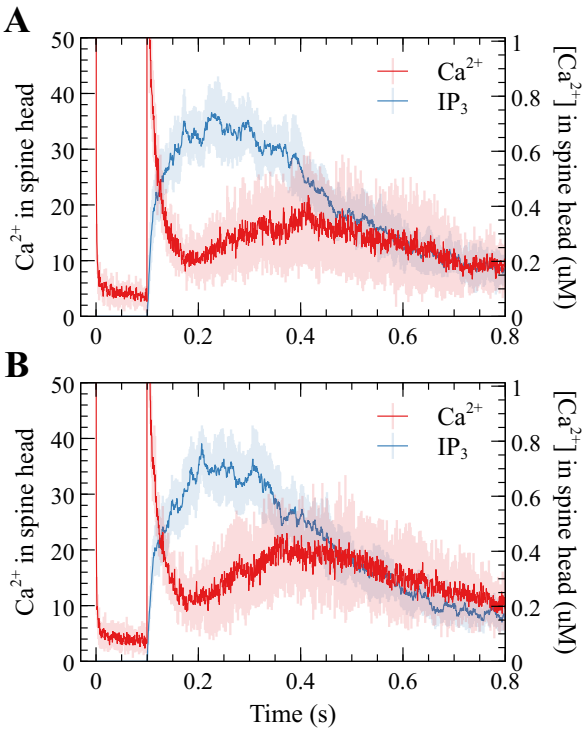

Figure S12: **(A, B)** Averages and standard deviations of 12 Ca^{2+} and IP_3 transients for a single PF stimulus with CF coactivation. Parameter sets B and C from Fig. 6 were used in (A) and (B), respectively. 380 caged IP_3 were used, resulting in a IP_3 transient with a peak value of approximately 1/5th of the peak used for the PF burst stimulus, see e.g. red plot in Fig. 9A. The resulting Ca^{2+} transients reach peak values of about 20 Ca^{2+} = 0.41 μM, in very good agreement with experimental estimates of 0.4 μM, see Piochon et al. (13).

1.7.5 Ataxia - Increasing IP_3

We vary the amount of IP_3 that is part of the PF stimulus and decrease the IP_3R's binding rate k_{on} of IP_3 from their standard values of $IP_{3,peak}$=4.5μM and k_{on} = 83.3 (μMs)$^{-1}$, resp., and investigate how much we need to increase IP_3 for a given decreased k_{on} to recover the usual values of the Ca^{2+} transients peak for the case of PF burst + CF stimuli.

We find that increasing the amount of IP_3 does increase the peak of the resulting Ca^{2+} transients for slower binding of IP_3, but it requires a lot more IP_3 to increase the peak values as required, Fig. S13. Even for peak values of IP_3 around 13μM we can only recover the Ca^{2+} transient's peak for an IP_3 binding rate of $k_{on} \approx 25$ (μMs)$^{-1}$. This significant increase of required IP_3 might quickly reach the saturation of the PLCβ pathway for intermediate to small values of k_{on}.

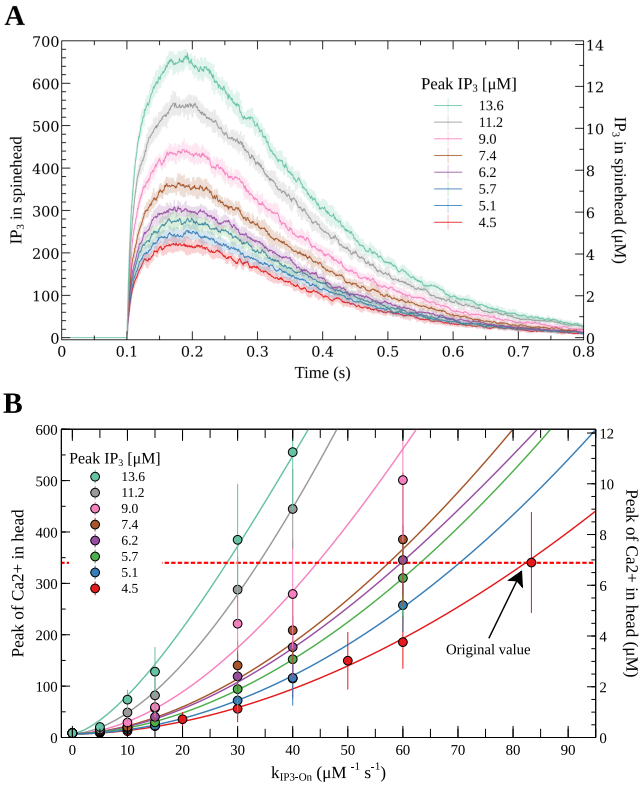

Figure S13: **(A)** Time courses of average [IP_3](t) in the spine head for different amounts of IP_3, **(B)** Values of Ca^{2+} transient peaks against binding rate of IP_3 for different amounts of IP_3. Red dotted line shows Ca^{2+} peak for standard values used in Fig. 7 in the main text.

SUPPORTING REFERENCES

1. Community, B. O., 2019. Blender - a 3D modelling and rendering package. Blender Foundation.

2. Stiles, J. R., D. V. Helden, T. M. B. Jr, E. E. Salpeter,

and M. M. Salpeter, 1996. Miniature endplate current rise times <100 μs from improved dual recordings can be modeled with passive acetylcholine diffusion from a synaptic vesicle. *Proc. Natl. Acad. Sci. USA* 5747–5752.

3. Stiles, J., and T. Bartol, 2001. Monte Carlo methods for simulating realistic synaptic microphysiology using MCell. *Computational Neuroscience: Realistic Modeling for Experimentalists* 87–127.

4. Kerr, R. A., T. M. Bartol, B. Kaminsky, M. Dittrich, J.-C. J. Chang, S. B. Baden, T. J. Sejnowski, and J. R. Stiles, 2008. Fast Monte Carlo Simulation Methods for Biological Reaction-Diffusion Systems in Solution and on Surfaces. *SIAM J Sci Comput* 30:3126.

5. Hoops, S., S. Sahle, R. Gauges, C. Lee, J. Pahle, N. Simus, M. Singhal, L. Xu, P. Mendes, and U. Kummer, 2006. COPASI—a COmplex PAthway SImulator. *Bioinformatics* 22:3067–3074.

6. Franks, K. M., and T. J. Sejnowski, 2002. Complexity of calcium signaling in synaptic spines. *BioEssays* 24:1130–1144.

7. Blackwell, K. T., 2013. Approaches and tools for modeling signaling pathways and calcium dynamics in neurons. *J. Neurosci. Methods* 220:131–140.

8. Moraru, I. I., E. J. Kaftan, B. E. Ehrlich, and J. Watras, 1999. Regulation of type 1 inositol 1,4,5-trisphosphate-gated calcium channels by InsP3 and calcium: Simulation of single channel kinetics based on ligand binding and electrophysiological analysis. *J. Gen. Physiol.* 113:837–49.

9. Doi, T., S. Kuroda, T. Michikawa, and M. Kawato, 2005. Inositol 1,4,5-Trisphosphate-Dependent Ca^{2+} Threshold Dynamics Detect Spike Timing in Cerebellar Purkinje Cells. *J. Neurosci.* 25:950–961.

10. Lee, S. H., B. Schwaller, and E. Neher, 2000. Kinetics of Ca^{2+} binding to parvalbumin in bovine chromaffin cells: implications for [Ca^{2+}] transients of neuronal dendrites. *J. Physiol.* 525 Pt 2:419–432.

11. Schmidt, H., K. M. Stiefel, P. Racay, B. Schwaller, and J. Eilers, 2003. Mutational analysis of dendritic Ca^{2+} kinetics in rodent Purkinje cells: role of parvalbumin and calbindin D28k. *J Physiol* 551:13–32.

12. Antunes, G., A. M. Sebastião, and F. M. Simoes De Souza, 2014. Mechanisms of regulation of olfactory transduction and adaptation in the olfactory cilium. *PLoS ONE* 9.

13. Piochon, C., H. K. Titley, D. H. Simmons, G. Grasselli, Y. Elgersma, and C. Hansel, 2016. Calcium threshold shift enables frequency-independent control of plasticity by an instructive signal. *PNAS* 113:13221–13226.

14. Stauffer, T. P., D. Guerini, and E. Carafoli, 1995. Tissue distribution of the four gene products of the plasma membrane Ca^{2+} pump. A study using specific antibodies. *J. Biol. Chem.* 270:12184–12190.

15. Lytton, J., M. Westlin, S. E. Burk, G. E. Shull, and D. H. MacLennan, 1992. Functional comparisons between isoforms of the sarcoplasmic or endoplasmic reticulum family of calcium pumps. *J. Biol. Chem.* 267:14483–14489.

16. Antunes, G., A. C. Roque, and F. M. Simoes-De-Souza, 2016. Stochastic Induction of Long-Term Potentiation and Long-Term Depression. *Sci. Rep.* 6:30899.

17. Harris, K. M., and J. K. Stevens, 1988. Dendritic spines of rat cerebellar Purkinje cells: serial electron microscopy with reference to their biophysical characteristics. *J. Neurosci.* 8:4455–69.

18. Airaksinen, M. S., J. Eilers, O. Garaschuk, H. Thoenen, A. Konnerth, and M. Meyer, 1997. Ataxia and altered dendritic calcium signaling in mice carrying a targeted null mutation of the calbindin D28k gene. *Proc. Natl. Acad. Sci. U.S.A.* 94:1488–1493.

19. Schmidt, H., and J. Eilers, 2009. Spine neck geometry determines spino-dendritic cross-talk in the presence of mobile endogenous calcium binding proteins. *J Comput Neurosci* 27:229–243.

20. Allbritton, N., T. Meyer, and L. Stryer, 1992. Range of messenger action of calcium ion and inositol 1,4,5-trisphosphate. *Science* 258:1812–1815.

21. Dickinson, G. D., K. L. Ellefsen, S. P. Dawson, J. E. Pearson, and I. Parker, 2016. Hindered cytoplasmic diffusion of inositol trisphosphate restricts its cellular range of action. *Sci. Signal.* 9:ra108–ra108.

22. Kakiuchi, S., S. Yasuda, R. Yamazaki, Y. Teshima, K. Kanda, R. Kakiuchi, and K. Sobue, 1982. Quantitative determinations of calmodulin in the supernatant and particulate fractions of mammalian tissues. *J. Biochem.* 92:1041–1048.

23. Takei, K., T. C. Siidhof, P. Volpe, and P. D. Camilw, 1992. Ca^{2+} Stores in Purkinje Neurons : Endoplasmic Reticulum Subcompartments Demonstrated by the Heterogeneous Distribution of the InsP , Receptor , Ca^{2+} -ATPase , and Calsequestrin. *J. Neurosci.* 12(2):189–505.

24. Wang, S. S., W. Denk, and M. Hausser, 2000. Coincidence detection in single dendritic spines mediated by calcium release. *Nat. Neurosci.* 3:1266–1273.